# Journal of Materials Chemistry A

Accepted Manuscript


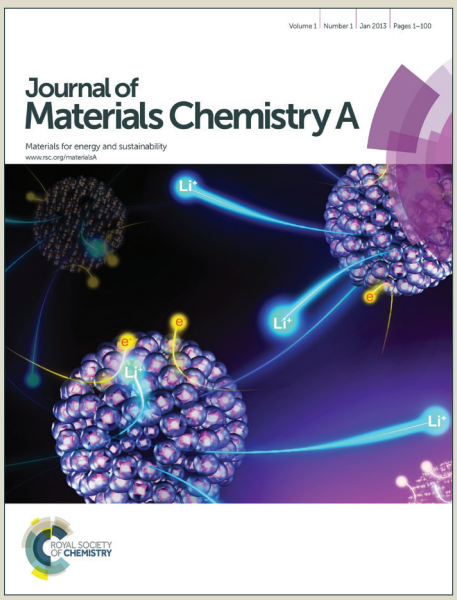





ROYAL SOCIETY OF CHEMISTRY

www.rsc.org/materialsA

A high rate and cycle performance $LiFe_{0.5}Mn_{0.5}PO_4/C$ material was obtained by synergies of surfactant-assisted solid state method and carbon content.

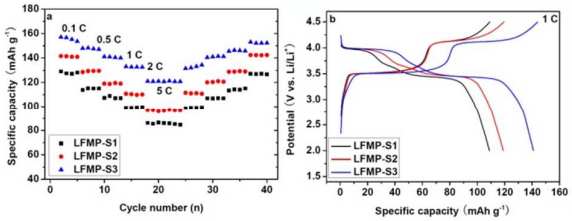

Cite this: DOI: 10.1039/c0xx00000x

www.rsc.org/xxxxxx

ARTICLE TYPE

# The Enhanced Rate Performance of $LiFe_{0.5}Mn_{0.5}PO_4$/C Cathode Material via Synergistic Strategies of Surfactant-assisted Solid State Method and Carbon Content

**Xue Zhou[a], Ye Xie[a], Yuanfu Deng*[a,b], Xusong Qin[b] and Guohua Chen*[b,c]**

***Received (in XXX, XXX) Xth XXXXXXXXX 200X, Accepted Xth XXXXXXXXX 200X***
**DOI: 10.1039/b000000x**

The rate performance of $LiMnPO_4$-based materials is further improved via synergistic strategies including surfactant-assisted solid state method, Fe-substitution and carbon-coating. The surfactant-assisted solid state strategy effectively decreases the primary particle size of the cathode material, which can greatly shorten the diffusion distance of lithium ion. The Fe-substitution improves the effectiveness of $Li^+$ insertion/extraction reactions in the solid phase. The uniform carbon coating layer and the conductive networks provided by the carbon between the nanoparticles ensure the continuous conductivity by the nanoparticles. As consequence of the synergistic effect, the as prepared $LiFe_{0.5}Mn_{0.5}PO_4$ sample with 6.10 wt% carbon exhibits a high specific capacity and superior rate performance with discharge capacities of 155.0, 140.9 and 121 mA h $g^{-1}$ at 0.1, 1 and 5 C (1 C = 170 $mAg^{-1}$), respectively. Meanwhile, it shows stable cycling stability at both room temperature (25 $^oC$, 94.8% and 90.8% capacity retention after 500 cycles at 1 and 5 C rates, respectively) and elevated temperature (55 $^oC$, 89.2% capacity retention after 300 cycles at 5 C rate). This material may have great potential application for advanced Li-ion batteries.

## Introduction

Lithium-ion batteries (LIBs) are dominating the market of portable electronics and their applications are expanding into electric vehicles (EVs) and hybrid electric vehicles (HEVs) over the past few decades.[1-3] In more recent years, $LiMnPO_4$ cathode material have attracted considerable attention as potential alternatives to commercial layered cathode materials for its superiorities on structural stability, cost effectiveness, environmental friendliness high-energy density, and compatibility with the major of commercial electrolytes.[4-6] However, its application in practical LIBs has been impeded by the low specific discharge capacity and the rather poor rate performance arising from its intrinsically low electric conductivity (< $10^{-10}$ S $cm^{-1}$) and ionic conductivity (< $10^{-16}$ $cm^2$ $s^{-1}$), and the poor capacity retention due to the dissolution of Mn during the cycling.[7-9]

Recent studies have demonstrated that the partial substitution of Mn with Fe in $LiMnPO_4$ can form $LiFe_xMn_{1-x}PO_4$ ($0 < x < 1$) solid solution with improved electronic and ionic conductivities and less Jahn-Teller effect.[10-29] The $x$ value should be large enough to keep the benefit of the higher electronic and ionic conductivity of the iron, but small enough to take the maximum benefit of the higher working potential with Mn.[6] Among them, the value of $x$ = 0.5 has become one of the most extensively studied examples in more recent years,[20-30] where an acceptable specific discharge capacity and rate performance can be obtained via carbon coating. For example, Muraliganth *et al.* synthesized $LiFe_{0.5}Mn_{0.5}PO_4$/C nanoparticles via high-energy mechanical milling (HEMM) approach.[20] This material shows a high specific discharge capacity of 148 mAh $g^{-1}$ at 0.05 C rate with high (20 wt%) conductive agent. However, no relative rate performance data was reported by the authors. Saravanan *et al.* prepared $LiFe_{0.5}Mn_{0.5}PO_4$/C nanoplates through a solvothermal route and thermal treatment.[21] This material shows specific discharge capacities of 121 and 103 at 0.1 and 2 C rates, respectively. Large amount of organic solvents were required in the synthesis process which may result in severe environment pollution. Hagen *et al.* prepared $LiFe_{0.5}Mn_{0.5}PO_4$/C nanofibers via electrospinning and thermal treatment at high temperature.[22] Only a moderate specific discharge of 110 mAh $g^{-1}$ was obtained at 0.5 C-rate by this material. Oh *et al.* synthesized micro-sized C-$LiFe_{0.5}Mn_{0.5}PO_4$ material with nanopores via co-precipitation route and two-steps thermal treatment.[23] This $LiFe_{0.5}Mn_{0.5}PO_4$/C microspheres show specific discharge capacities of 142 and 120 mAh $g^{-1}$ at 0.05 and 0.5 C rates, respectively. Xiao *et al.* synthesized $LiFe_{0.5}Mn_{0.5}PO_4$/C nanoparticles via a polymer-assisted mechanical activation (PAMA) route.[24] A high specific capacity and good rate performance (~ 150 and ~ 120 mAh $g^{-1}$ at 0.2 and 10 C rates, respectively) were achieved by the $LiFe_{0.5}Mn_{0.5}PO_4$/C nanoparticles. Despite high specific capacities were obtained of the two above-mentioned cathode materials, the columbic efficiency of these two materials is low because the constant current–constant voltage mode was applied during the cycling. Zhong *et al.* prepared $LiFe_{0.5}Mn_{0.5}PO_4$/C with a reversible capacity of 138 mAh $g^{-1}$ at 0.1 C rate by rheological phase reaction using five respective raw materials.[25] These many

starting precursors may bring inhomogeneous composition distribution of the final product in the practical application. Zong *et al*. prepared $LiFe_{0.5}Mn_{0.5}PO_4/C$ using the flake-like $Mn(PO_3(OH))\cdot 3H_2O$ precursor,[26] which shows a specific capacity of 131 mAh $g^{-1}$ at 0.05 C rate. Paolella *et al*. reported the colloidal synthesis of $LiFe_{0.5}Mn_{0.5}PO_4$ platelet-shaped nanocrystal and observed a single broad peak in its cyclic voltammetry, but they did not report the charge/discharge performance in the literature.[27] More recently, $LiFe_{0.5}Mn_{0.5}PO_4$ or $LiFe_{0.5}Mn_{0.5}PO_4/C$ with the different morphologies have also been synthesized from hydrothermal route,[28-30] however, the material shows disappointing electrochemical properties due to defects in the crystal structure when synthesized hydrothermally at low temperatures. Based on the analysis of the above mentioned investigation results, irrespective of many synthesis methods employed, it is clearly seen that the reduction of the particle size and the high temperature thermal treatment of carbon-coated $LiFe_{0.5}Mn_{0.5}PO_4$ for achieving good crystallization of the phase are very crucial to obtain high specific discharge capacity and good rate performance.

Solid-state synthesis is the most "robust" and conventional method used industrially to synthesize powder materials for lithium batteries because of its (apparent) simplicity, ideal for continuous large-scale production. Furthermore, choosing reasonable raw materials and carbon sources are also very key factors for large scale production of the objective materials. However, for the case of $LiMnPO_4$-based cathode materials, it is still a very big challenge because the conventional solid state synthesis route usually causes big particle size at high temperature calcination. Therefore, to develop a novel, inexpensive and high-efficiency solid state synthesis route for large scale production of $LiMnPO_4$-based cathode materials with small particle size, uniform carbon layer, and good electrochemical properties is very urgent and necessary.

Herein, we prepare $LiFe_{0.5}Mn_{0.5}PO_4$ nanoparticles with different carbon content via a facile surfactant-assisted solid state route in the first time, which was designed to synthesis high performance of $LiMnPO_4/C$[31-33] and $LiFe_{0.15}Mn_{0.85}PO_4/C$ cathode materials.[34] Selection of $LiFe_{0.5}Mn_{0.5}PO_4$ acts as a new object of study because the rate performances of the $LiMnPO_4/C$ and $LiFe_{0.15}Mn_{0.85}PO_4/C$ cathode materials synthesized by this method need to be improved.[31-34] The effect of surfactant (oleic acid) and carbon content on the particle size and the electrochemical performance of the obtained $LiFe_{0.5}Mn_{0.5}PO_4/C$ materials were investigated in detail. Different from the previous investigation on the effect of the carbon content on the conductivity of the $LiMnPO_4$-based cathode material,[33-35] the underlying reason of the improvement of the electrochemical performance of the obtained $LiFe_{0.5}Mn_{0.5}PO_4/C$ material by increasing of the carbon content was attributed to the synergistic effect of particle size reduction and the improvement of conductivity. The as prepared $LiFe_{0.5}Mn_{0.5}PO_4$ cathode with 6.10 wt% carbon exhibits a high specific capacity, superior rate performance and excellent cycling performance. Such as $LiMn_{0.5}Fe_{0.5}PO_4/C$ may act as a good option for high-power applications such as EV/HEVs that are keen on rapid charge and durability.

## Experimental

**Preparation of $Fe_{0.5}Mn_{0.5}C_2O_4\cdot 2H_2O$**: Homogenous bimetallic metal oxalate ($Fe_{0.5}Mn_{0.5}C_2O_4\cdot 2H_2O$) was prepared by the similarly procedure in the literatures.[18,34] In a typical experiment, $MnSO_4\cdot 4H_2O$ (2.2306 g, AR, Aladdin Chemical Agents Co. Ltd) and $FeSO_4\cdot 7H_2O$ (2.7802 g, AR, Aladdin Chemical Agents Co. Ltd) were dissolved in water successively to prepare 20 ml of bimetallic sulphate solution (0.5 M in $MnSO_4$ and $FeSO_4$, respectively). After that, 41 mL of sodium oxalate solution (0.5 M) was added into the bimetallic sulphate solution quickly under continuous stirring and a $N_2$ atmosphere. The stirring was maintained for 15 minutes. Bright yellow particles were then collected via filtration, washed with distilled water three times, and dried in a vacuum oven at 60 $^oC$ for 10 h to obtain the $Fe_{0.5}Mn_{0.5}C_2O_4\cdot 2H_2O$ product.

**Preparation of $LiFe_{0.5}Mn_{0.5}PO_4/C$ (LFMP-S1)**: In a typical experiment, stoichiometric amounts of $LiH_2PO_4$ (1.0393 g, AR, Aladdin Chemical Agents Co. Ltd), $Fe_{0.5}Mn_{0.5}C_2O_4\cdot 2H_2O$ (1.7944 g) and phenolic resin (0.0787 g, AR, Shanghai Chemical Agents Co. Ltd) were mixed in ethanol (AR, Guangzhou Chemical agents Co. Ltd) and then ball-milled for 4 h at 400 RPM. The mixtures were dried under vacuum for 6 h at 80 $^oC$ and then transferred to a tube furnace for calcination at 250 °C for 2 h under an Ar atmosphere. After that, the calcination temperature was raised to 600 °C and then kept for additional 10 h to obtain carbon coating $LiFe_{0.5}Mn_{0.5}PO_4$ composite.

**Preparation of $LiFe_{0.5}Mn_{0.5}PO_4/C$ (LFMP-S2)**: This material was synthesized by an oleic acid-assisted solid-state synthesis route.[33,34] The synthesis procedures were similar to those of LFMP-S1except 1.5 g of oleic acid (AR, Shanghai Chemical Agents Co. Ltd) was added into the precursors when they were ball-milling.

**Preparation of $LiFe_{0.5}Mn_{0.5}PO_4/C$ (LFMP-S3)**: The LFMP-S3 sample with different carbon content from LFMP-S2 was synthesized using the same procedures as those of LFMP-S2 except 0.1300 g of phenolic resin were used as carbon source.

**Physical characterizations**

The crystalline structure and particle morphology of $LiFe_{0.5}Mn_{0.5}PO_4/C$ samples were characterized by X-ray diffraction (XRD) (Bruker D8 ADVANCE, Cu Kα radiation, λ = 1.5406 Å), scanning electron microscopy (SEM, JEOL 6300F) and transmission electron microscopy (TEM, PHILIPS TECNAI F30). Raman spectrum was obtained with a Bio-Rad FTS6000 Raman spectroscopy with a 532 nm blue laser beam. Fourier transform infrared (FT-IR) spectrum was recorded with KBr pellets using a Bruker R 200-L spectrophotometer. The carbon contents of all of the $LiMn_{0.5}Fe_{0.5}PO_4/C$ samples were determined by an elemental analyzer (Vario EL III, Elemental Analysensystem). The compositions of the obtained samples were tested by Energy Dispersive Spectrometer (EDS) analysis on MERLIN FE-SEM.

**Electrochemical studies**

To evaluate the electrochemical performance of the obtained samples, electrodes consisting of 80 wt% $LiFe_{0.5}Mn_{0.5}PO_4/C$, 10 wt% acetylene black and 10 wt% polyvinylidene fluoride (PVDF) were prepared on aluminium foil by a tape-casting technique. Coin cells (CR2025) were assembled using the prepared $LiFe_{0.5}Mn_{0.5}PO_4/C$ electrode as cathode, lithium metal foil as

anode, 1.0 M $LiPF_6$ solution in ethylene carbonate/ethylene methyl carbonate (EC : EMC = 1:1 v/v) as electrolyte and Celgard 2400 as separator in an Ar-filled glove box (MBRAUN LAB MASTER130). The loading of the active material in the electrode was ca. ~ 2 mg $cm^{-2}$. The fabricated cells were cycled in the voltage range between 2.0 and 4.5 V vs. $Li/Li^+$ at different current rates on a multichannel battery test system (NEWARE CT-3008W) using a constant current charge-discharge mode. The cyclic voltammetry (CV) measurement was performed on an electrochemical workstation (AUTOLAB PGSTAT 101) at different scan rate in the range of 2.0–4.5 V vs. $Li/Li^+$. The electrochemical impedance spectroscopy (EIS) data of the electrodes were acquired at room temperature using a Zahner-elektrik IM6 electrochemical workstation #12481 (made in Germany) before cycling in the frequency ranging from 100 kHz to 10 mHz by imposing an alternate current with an amplitude of 10 mV on the electrode. The specific capacity in the paper is based on the mass of the $LiFe_{0.5}Mn_{0.5}PO_4$/C composite.

## Results and discussion

Fig. 1 shows the XRD patterns of the obtained three $LiFe_{0.5}Mn_{0.5}PO_4$/C samples. All peaks can be well indexed based on a single phase olivine-type structure in orthorhombic with a *pnmb* space group (JCPDS No. 42-0580). No peaks of impurity phases were found in the three samples. Moreover, no obvious carbon was observed in the LFMP-S1 and LFMP-S2 samples, which is attributed to the low content and amorphous structure of carbon coating layer. However, a broad peak was observed in the LFMP-S3 in the $2\theta$ = 20 ~ 30°, which may be attributed to a higher carbon content in this sample. The carbon contents, originating from the elemental analysis, are 3.68, 3.73 and 6.10 wt% in the LFMP-S1, LFMP-S2 and LFMP-S3, respectively. The lattice parameters of LFMP-S1 are $a$ = 6.032(8), $b$ = 10.375(9) and $c$ = 4.713 (5) Å, respectively, based on the calculation (MDI Jade 5.0 software). These values are consistent with the calculated results of LFMP-S2 $a$ = 6.037(5), $b$ = 10.370(5) and $c$ = 4.715(3) [Å] and LFMP-S3 [$a$ = 6.044(8), $b$ = 10.369 (9) and $c$ = 4.720 (4) Å]. The crystallite sizes are 67.4 × 74.2 × 50.2 and 39.1 × 38.1 × 35.5 nm for LFMP-S2 and LFMP-S3, respectively, which were calculated using the Debye–Scherrer formula [$D = K\lambda/(\beta\cos\theta)$; where K is the Scherrer constant (close to 0.9), λ is the X-ray wavelength of Cu Kα = 1.54178 nm), β is the full width at half-maximum (FWHM) intensity of the prominent (1 1 1), (1 2 1) and ( 1 3 1) reflections in radian, and θ is the Bragg diffraction angle.[36] Because of the big particle size of LFMP-S1 (> 100 nm), the crystallite size for LFMP-S1 is not suitable for calculation using the Debye–Scherrer formula. In addition, the compositions of the three samples were tested by EDS analysis and the characterization results were listed in the supporting information (Table S1).

Fig. 2a displays the FT-IR spectra of the obtained three $LiFe_{0.5}Mn_{0.5}PO_4$/C samples in the 1300−400 $cm^{-1}$ corresponding to the vibrations mode of $PO_4^{3-}$ anion. All of the three samples show similar vibration modes. The three peaks at 1139, 1093 and 1057 $cm^{-1}$ are attributed to the asymmetric stretching mode ($\nu_3$). The bands at 983 and 638 $cm^{-1}$ are ascribed to symmetric stretching mode ($\nu_1$) and asymmetric bending mode ($\nu_4$). The four bands at 581, 549, 507 and 465 $cm^{-1}$ correspond to the bending modes ($\nu_2$ and $\nu_4$).[25,37] It is worthwhile noting that the band of bending mode $\nu_1$ which indicates the deformation of P−O, is in the range of that for $LiFePO_4$[38] (979 $cm^{-1}$) and $LiMnPO_4$[39] (989 $cm^{-1}$), revealing the homogenous distribution of iron and manganese in the $LiFe_{0.5}Mn_{0.5}PO_4$ solid solution.

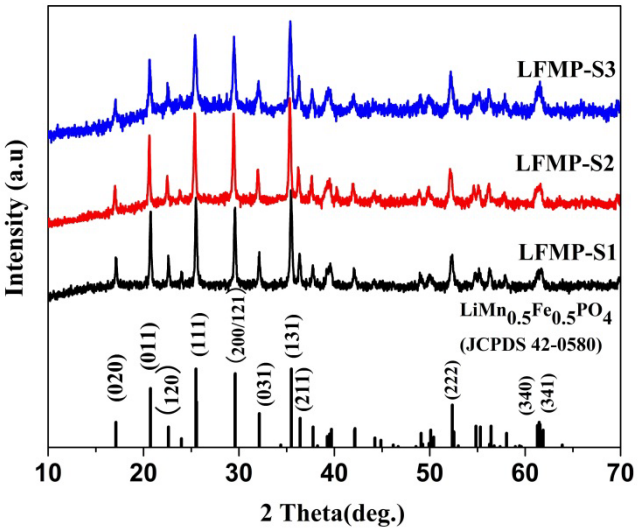


Fig. 1. XRD patterns of the obtained three $LiFe_{0.5}Mn_{0.5}PO_4$/C composites.

Raman experiments can present the chemical signal in the surface region and are extensively sensitive to the surface species due to the limited penetration depth of the incident laser into the sample. To detect the surface composition of the three $LiFe_{0.5}Mn_{0.5}PO_4$/C samples, we measured Raman spectra of these three samples, as shown in Fig. 2b. The Raman signals of these three samples displayed two strong and broad peaks at about 1330 and 1590 $cm^{-1}$, which are attributed to the D band (disordered carbon) and G band (graphite) for amorphous carbon, respectively.[40] Despite the same carbon precursor (phenolic resin) was used for preparation of the three samples, the peak intensity ratios ($I_D/I_G$) of the three samples are some different (0.92, 1.05 and 1.23 for LFMP-S1, LFMP-S2 and LFMP-S3, respectively). An increase in the $I_D/I_G$ ratio was observed with the decrease of the particle size, which may due to the formation of more defects in the carbon coating of LFMP-S3.[41] By carefully comparing these three Raman spectra, we can find a distinct difference in the range of 800–1000 $cm^{-1}$. A weak Raman peaks around 950 $cm^{-1}$ can be detected for LFMP-S1, assigning to the character of $PO_4^{3-}$ anion,[40] which may be attributed to the inhomogeneous distribution of carbon layer on the LFMP-S1 particles. These results suggest that the oleic acid has important roles in restricting the particle size and distributing homogenously the carbon precursor. In addition, no obvious Raman signals at 950 $cm^{-1}$ can be distinguished in the LFMP-S3 sample, suggesting that the thickly coated carbon (6.10 wt%) may screen the deeper LFMP-S3 from being detected.[40] The uniform distribution of carbon on the surface of primary $LiFe_{0.5}Mn_{0.5}PO_4$ particles was further demonstrated by the HTEM image (Fig. 3g and Fig. S1) and EDS mapping analysis (Fig. S2).

Fig. 3 shows the SEM images of LFMP synthesized at different experimental condition. All of the three samples were composed of agglomerated nanoparticles. However, by carefully comparing these SEM images, some difference of the primary

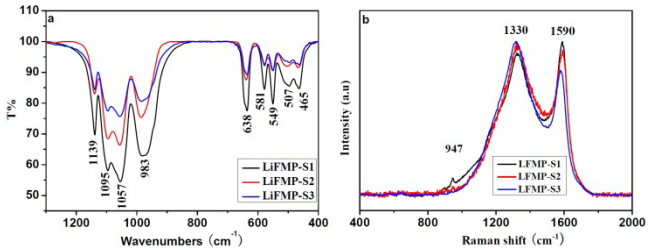


Fig. 2. (a) FT-IR and (b) Raman spectra of the three $LiFe_{0.5}Mn_{0.5}PO_4/C$ composites.

particle size and the agglomerated morphology can be distinguished. For the case of LFMP-S3, a narrow size distribution and a lot of pores in the loosely agglomerated structure were found (as shown in Fig. 3d in large magnification), which suggested that both of the oleic acid and the carbon content have important effect on the particle sizes and morphologies of the as-prepared materials. The morphology of the as-synthesized material is similar to those prepared by the solid state reaction.[33,34] Figs. 3e and 3f show the TEM and HTEM images of the LFMP-S3. As shown in Fig. 3e, the size of the LFMP-S3 particles distributed in narrow range of 35-70 nm, and they are loosely connected and separated by carbon with some voids existing between them. These voids are benefit for electrolyte infiltration and storage, which will improve the rate performance of the sample. Further investigation on the structure features of the LFMP-S3 nanoparticles was by HRTEM, as shown in Figs. 3f and 3g. It can be clearly seen that the primary nanoparticles are embedded in a carbon matrix. Clear atomic lattice of the sample could be found in Fig. 3g, revealing good crystallinity of the LFMP-S3 sample. The lattice fringes with a width of 2.53 Å well correspond to the d-spacing of (131) crystal planes of a typical $LiFe_{0.5}Mn_{0.5}PO_4$ crystal. An amorphous phase of carbon layer with a thickness of around 5 nm covered uniformly on the surface of primary particle. Meanwhile, the thickness of the carbon network is dependent on the content of carbon precursor. When a small amount of phenolic resin (0.0787 g) was added, big particle sizes and thin carbon layer the LFMP-S2 are observed (as shown in Fig. S3). Furthermore, the primary particles tightly overlapped each other and some pores in the agglomerated structure. In contrast, traditional LFMP-S1 synthesized through the same procedure without the assistance of the oleic acid exhibits totally different architecture. The size of primary $LiFe_{0.5}Mn_{0.5}PO_4$ particles distributed in a wide range of 50–500 nm and almost no pores were found in the tightly agglomerated structures (Fig. S4). These results suggested that both of the oleic acid and the carbon content play important role in controlling the particle size and the agglomerated structure. The oleic acid-assisted solid state synthesis route is an effective method for uniform distribution of carbon coating layer and the formation of the hierarchical structure of $LiFe_{0.5}Mn_{0.5}PO_4$ nanoparticles.

The detail electrochemical properties of the three samples as cathode material for LIBs were investigated by galvanostatic charge-discharge tests, cyclic voltammetry (CV), and electrochemical impedance spectroscopy (EIS). Fig. 4a shows the first charge-discharge curves (C-D Cvs) of the LFMP-S1, LFMP-S2 and LFMP-S3 electrodes at 0.1 C rate (1 C = 170 mA $g^{-1}$). All of the three materials exhibited two typical discharge voltage plateaus about at 4.0 and 3.4 V vs. $Li/Li^+$, corresponding

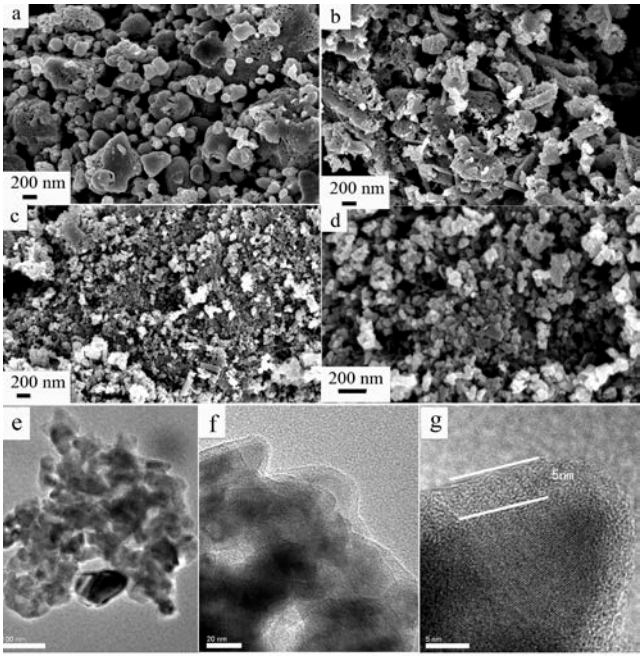


Fig. 3. SEM and TEM images of the as-synthesized LFMP-based materials. SEM images of (a) LFMP-S1, (b) LFMP-S2 and (c), (d) LFMP-S3. TEM images (e) and (f) and HRTEM (g) of LFMP-S3.

respectively to the redox plateau potentials of $Mn^{2+}/Mn^{3+}$ and $Fe^{2+}/Fe^{3+}$.[14,19] The specific discharge capacities of 130, 144 and 155 mAh $g^{-1}$ were obtained for LFMP-S1, LFMP-S2 and LFMP-S3, respectively. High columbic efficiencies of 90.8, 92.7 and 96.3% for respective LFMP-S1, LFMP-S2 and LFMP-S3 were observed. Some minor differences including the voltage plateaus and the polarization potential were found except the specific capacities in the charge-discharge curves, which were also verified by the CV results, as shown in Fig. 4b. In the first CV curves of the three materials, the LFMP-S3 exhibits the strongest and well-defined oxidation and reduction peaks. The LFMP-S3 shows the narrowest potential intervals between the oxidation and reduction peaks (0.09 V for $Fe^{2+}/Fe^{3+}$ and 0.16 V for $Mn^{2+}/Mn^{3+}$, respectively), which suggest that it has the best kinetic for lithium ions to insert into and extract from $LiFe_{0.5}Mn_{0.5}PO_4$. These potential intervals are smaller than those of the recently reported $LiFe_{0.5}Mn_{0.5}PO_4/C$ material with the highest specific capacity.[23] Furthermore, the well superposition of the CVs after the first cycle indicates the excellent cycling performance of LFMP-S3 (Fig. 4c). In comparison, the largest over-potentials (0.11 V for $Fe^{2+}/Fe^{3+}$ and 0.20 V for $Mn^{2+}/Mn^{3+}$, respectively) and lowest peak current of LFMP-S1 indicate the slowest kinetic of this composite in the three materials. The improvement of the kinetic for lithium ions to insert into and extract from LFMP-S3 may indicate that the oleic acid-assisted solid state route for the preparation of $LiFe_{0.5}Mn_{0.5}PO_4$ sample with suitable carbon content is a good strategy for high performance $LiMnPO_4$-based cathode materials.

The rate performance of the three obtained samples is depicted in Fig. 5a. For the rate test, the cells were charged at different rates (from 0.1 to 5 C rates) and discharged at the corresponding rates, respectively. As expected, the LFMP-S3 displayed the best rate capability. It delivered average reversible specific capacities of 155, 147, 140, 132, and 120 mAh $g^{-1}$ at 0.1, 0.5, 1, 2 and 5 C

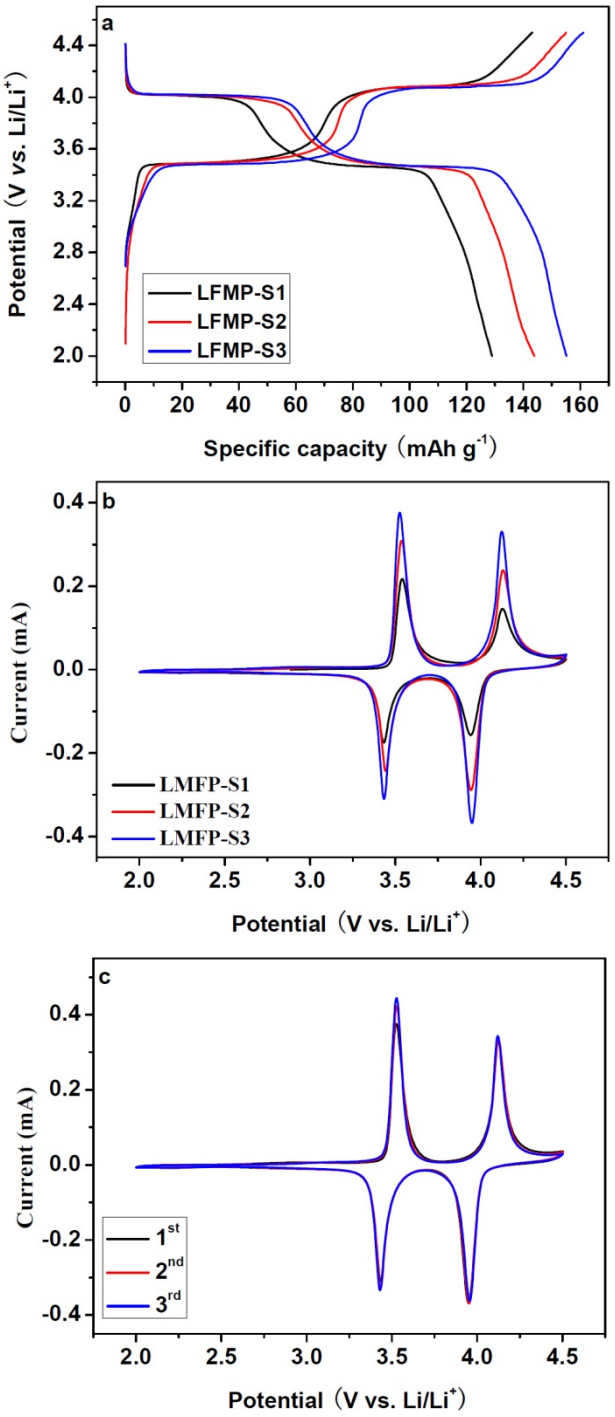


Fig. 4. (a) Charge-discharge curves at 0.1 C (1 C = 170 mA $g^{-1}$) and (b) Cyclic voltammograms (CVs) at a scan rate of 0.1 mV $s^{-1}$ of the three $LiFe_{0.5}Mn_{0.5}PO_4$/C composites and (c) CVs of the first three cycles of LFMP-S3.

rates (from 0.1 to 5 C rates) and discharged at the corresponding rates, respectively. As expected, the LFMP-S3 displayed the best rate capability. It delivered average reversible specific capacities of 155, 147, 140, 132, and 120 mAh $g^{-1}$ at 0.1, 0.5, 1, 2 and 5 C rates, respectively. For the LFMP-S2, the corresponding specific capacities are 143, 130, 120, 110 and 98 mAh $g^{-1}$ at 0.1, 0.5, 1, 2 and 5 C rates, respectively. For the LFMP-S1, the corresponding specific capacities are only 130, 115, 107, 98 and 85 mAh $g^{-1}$ at 0.1, 0.5, 1, 2 and 5 C rates, respectively. It is quite impressed that even after charging/discharging at high current densities; the reversible specific capacities could still be recovered to 127, 143 and 153 mAh $g^{-1}$ for respective LMFP-S1, LMFP-S2 and LMFP-S3 when the current density was reduced to 0.1 C. This clearly demonstrates the excellent current rate tolerance capability of the three materials. The high rate performance for LFMP-S3 is better or comparable to the state-of-art $LiFe_{0.5}Mn_{0.5}PO_4$-based cathode materials (as shown in Table S2).[21-26] Figs. 5b and 5c show the comparison of the charge-discharge curves of the three materials at 1 and 5 C rates, respectively. With the increase of charge-discharge current, the potential gaps for the three samples between the oxidation and reduction peaks became obvious. Fig. 5d shows the discharge curves of LFMP-S3 at different charge-discharge rates. The profiles at low charge/discharge rate (0.1 C) clearly show two distinguished plateaus located at about 4.0 and 3.5 V versus $Li/Li^+$. When the charge–discharge rate was increased to 5 C, separation of the two discharge plateaus gradually became blurred and the plateau voltages shifted to lower values due to the increased cell polarization at very high current density. Compared to the previous reports,[21-26] the LFMP-S3 composite synthesized in the present study shows a comparable/higher specific discharge capacity at high discharge voltages (> 3.5 V) when it is cycled at high current rates, indicating that higher or comparable energy density could be achieved. The superior rate performance of the LFMP-S3 is mainly attributed to the improved electronic and conductivity arising from the reasonable carbon content and the 3D conductive network (as shown in the TEM images) and fast lithium ion diffusion due to the greatly shorten diffusion path.

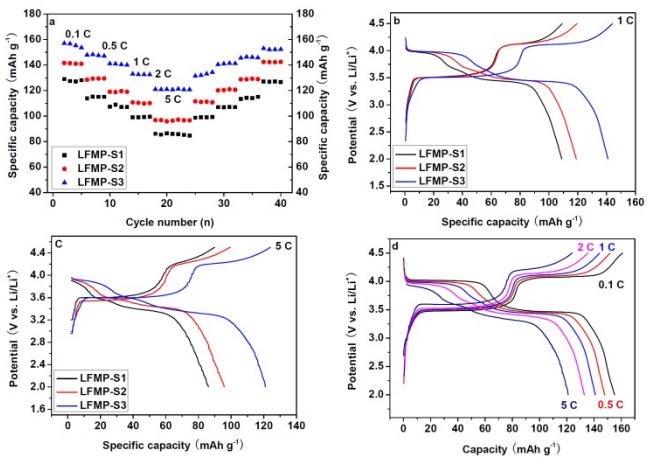


Fig. 5. Comparisons of (a) the rate performance at different C-rate, (b) Charge-discharge curves at 1 C-rate, and (c) Charge-discharge curves at 5 C-rate for the three $LiFe_{0.5}Mn_{0.5}PO_4$/C composites, and (d) charge-discharge curves of the LFMP-S3 composite at different C-rates.

The cycle performances of the as-obtained LFMP-S3 at different current densities (1 and 5 C) charge/discharge are respectively shown in Figs. 6a and 6b. The corresponding charge/discharge curves of selected cycles were also displayed in Fig. 6c and 6d, respectively. This $LiFe_{0.5}Mn_{0.5}PO_4$/C composite showed initial capacities of 139 and 120 mAh $g^{-1}$ at 1 and 5 C, respectively. The capacity retention capability of 95% and 91 was obtained after 500 cycles at 1 and 5 C, respectively, with Columbic efficiencies of near 100% after the first several cycles.

As shown in Figs. 6c and 6d, one may notice that the discharge voltage plateau as 4.0 V corresponding to $Mn^{2+}/Mn^{3+}$ redox reaction becomes shorter with current density increased. However, the discharge voltage plateau at 3.5 V which corresponds to $Fe^{2+}/Fe^{3+}$ redox reaction was almost same. This fact suggested that the greater polarization appeared to $Mn^{2+}/Mn^{3+}$ rather than $Fe^{2+}/Fe^{3+}$ as current density increased. Despite the discharge plateau of 4.0 V became some shorter after long cycles at high current density, only negligible discharge capacity loss at above 3.5 V, attributing the reduction of $Mn^{3+}$ to $Mn^{2+}$, was found. This phenomenon is not consistent with that of the recently reported $LiFe_{0.5}Mn_{0.5}PO_4/C$ microspheres,[14] in which the discharge capacity loss occurred mainly at above 3.5 V with increased current density and cycle number. The authors suggested that the capacity loss of $LiFe_{0.5}Mn_{0.5}PO_4/C$ microspheres was mainly due to the dissolution of Mn in the electrolyte during the long cycling. The small discharge capacity loss at above 3.5 V of the LFMP-S3 sample synthesized in the present study is probably attributed to the uniform distribution of carbon coating layer on the surface of primary $LiFe_{0.5}Mn_{0.5}PO_4$ particles (as demonstrated by the TEM image and Raman spectrum), which plays a key role in suppressing the surface reactivity between the charged electrode and the electrolyte and decreasing the Mn dissolution. In addition, good capacity retention capability was also achieved by the LFMP-S2 sample at different charge-discharge current densities (as shown in Fig. S5). It shows initial capacities of 121 and 99 mAh $g^{-1}$ at 1 and 5 C, respectively. The corresponding capacity retention is 93% and 92% after 500 cycles.

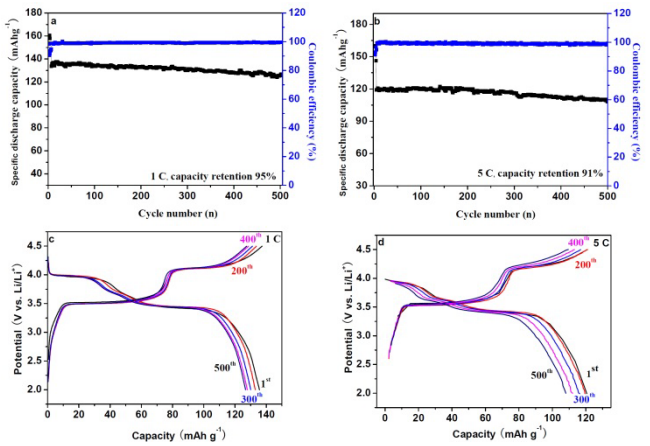


**Fig. 6**. (a) Cycling performance at 1 C, (b) 5 C-rate, (c) Charge-discharge curves of selective cycles at 1 C and (d) 5 C rate of the LFMP-S3 composite.

To evaluate the cycle performance at elevated temperature, the as-prepared LFMP-S3 sample was cycled at 5 C rate and 55 °C after activation two cycles at 25 °C and 0.5 C rate. As shown in Fig. 7a, this cathode material displayed an initial specific discharge capacity of 147.5 mAh $g^{-1}$, with 89% capacity retention capability after 300 cycles. In comparison with the charge/discharge curves at the same current density and different temperatures (25 and 55 °C, as shown in Fig. 6d and Fig. 7b, respectively), it was found that the increased discharge capacity appeared mainly in the 4.0 V region. This observation showed that the specific discharge capacity of the $LiMn_{1-x}Fe_xPO_4$-based materials can be improved at elevated temperature because of the faster $Li^+$ diffusion induced by the elevated temperature. Similar experimental results were also reported in literatures.[23,24] To the best of our knowledge, the good capacity retention capability of LFMP-S3 is comparable to the best result for the nanostructured $LiFe_{0.5}Mn_{0.5}PO_4/C$ material in the recently literature.[23] The good cycling performance at elevated temperature, a critical parameter for the cathode material valuation, of the as-prepared cathode material may also demonstrate that this $LiMn_{0.5}Fe_{0.5}PO_4/C$ composite (LFMP-S3) is a promising cathode material for high performance LIBs.

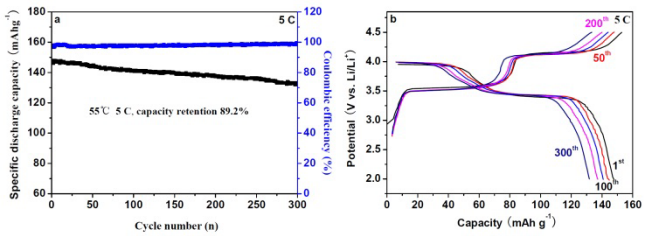


Fig. 7. (a) Cycling performance at 5 C rate and 55 °C and (b) Charge-discharge curves of the selective cycles at 5 C rate and 55 °C of the LFMP-S3 composite.

The EIS tests of coin cells were carried out to further demonstrated the difference in the electrochemical activity of the three $LiMn_{0.5}Fe_{0.5}PO_4/C$ composites, as shown in Fig. 8. The impedance spectra can be demonstrated on the basis of an equivalent circuit (as shown in the inset of 8).[42,43] It is apparently seen that all of the three EIS spectra are composed of a small intercept in the high frequency, a depressed semicircle at high-to-medium frequency and an inclined line in the low frequency regions. The high frequency intercepts refer to uncompensated resistance ($R_u$). $R_u$ includes the particle-particle contact resistance, electrolyte resistance and the resistance between the electrode and the current collector.[44] The dimensions of the depressed semicircles correspond to the charge transfer resistances ($R_{ct}$) at electrode/electrolyte,[33,44] which are 38.5, 30.3 and 26.8 Ω for LFMP-S1, LFMP-S2 and LFMP-S3, respectively. The lower the charge-transfer resistance, the higher the rate performances are. [45] The lowest $R_{ct}$ of LFMP-S3 indicates that the best electronic conductivity due to the highest carbon content, which facilitates greatly the reaction kinetics at the interface. The inclined lines in the low frequency are attributed to of the Warburg impedance ($W_o$), which is associated with the lithium ions diffusion in the electrodes.

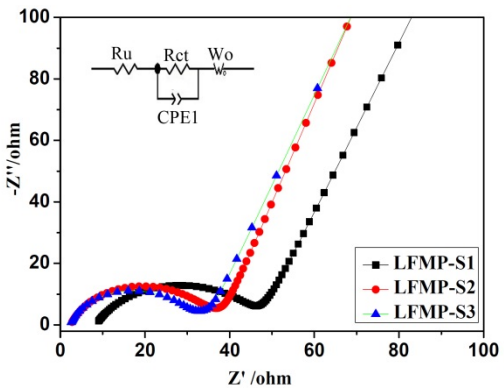


**Fig. 8**. Impedance spectra of the coin cells made with the three $LiFe_{0.5}Mn_{0.5}PO_4/C$ composites, respectively.

In order to gain a better understanding of the factors leading to the high rate performance of the LFMP-S3 electrode, a series of voltammetry measurements were tested. The CV results of the LFMP-S3 coin cells at different sweeping rates show two obvious redox peaks which can be observed even for the highest sweeping rate of 0.5 mV $s^{-1}$ (Fig. 9a). The two redox peaks are also consistent with the observed two-plateau charge–discharge profiles at low rate (0.1 and 0.5 C). It is noted that a small redox peak (~ 3.6 V) was observed in the CV scanned at 1.0 mV $s^{-1}$, which corresponds to the small discharge plateau at ~ 3.6 V when the cell was cycled at 1.0 C rate (Fig. 5 c). In addition, the LFMP-S3 electrode displays increasing peak current density ($I_p$) and widening separation potential within each redox couple as the potential scanning rate ($v$) increases, similar to the electrode prepared from $LiFePO_4$/C.[44,46] Based on the previous results, the peak current ($I_p$) of spherical electrodes for Li-ion diffusion coefficient ($D_{Li}$) can be estimated based on the Randles Sevcik equation:[47]

$$I_p = (2.69 \times 10^5) A\, C_{Li} D_{Li}^{1/2} n^{3/2} v^{1/2}$$

Where $A$ is the surface of area of the electrode, $C_{Li}$ is the bulk concentration in moles per cubic centimeter (~ 0.0228 mol·$cm^{-3}$), $D_{Li}$ is the diffusion coefficient in square centimeters per second, $n$ is the number of electrons per reaction species, and $v$ is the potential scan rate in volts per second. For a given charge number, the $D_{Li}$ can be calculated from the slope of peak current versus the square root of the scan rate ($v^{1/2}$) (Fig. 9b). The results are summarized in Table 1. The diffusion coefficients for the four different peaks are very similar, ranging from $1.72 \times 10^{-11}$ to $1.1 \times 10^{-10}$ $cm^2$ $s^{-1}$. These values are between the ones calculated for Li-ion diffusivity for $LiFePO_4$/C nanoparticles ($6.4 \times 10^{-10}$)[46] and $LiMnPO_4$/C nanocomposite ($6.6 \times 10^{-13}$).[33] The improved lithium ion diffusion coefficients in the Mn regime of the LFMP-S3 imply that Fe-doped $LiMnPO_4$ cathode material favors faster lithium ion intercalation kinetics, resulting in its high rate performance. In addition, the diffusion coefficients of LFMP-S3 are much larger than those of the LFMP-S2 ($6.0\times 10^{-12}$ to $3.29 \times 10^{-11}$ $cm^2$ $s^{-1}$) and LFMP-S1 ($4.8\times 10^{-12}$ to $3.2 \times 10^{-11}$ $cm^2$ $s^{-1}$), which is also a good case for explanation the best rate performance of the LFMP-S3.

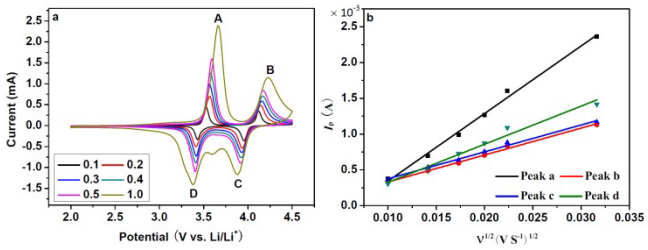


**Fig. 9**. The CVs at different scan rates for the coin cell made with LFMP-S3 composite.

## Conclusions

In summary, three $LiMn_{0.5}Fe_{0.5}PO_4$/C cathode materials with different carbon contents and particle sizes were successfully prepared by a surfactant-assisted solid-state method. The effects of the oleic acid and carbon content on the particle sizes and electrochemical performance were explored. The results demonstrated that the oleic acid and high carbon content could efficiently decrease the particle size and improve the electrochemical activity. Electrochemical tests showed that the as-prepared nanometer $LiMn_{0.5}Fe_{0.5}PO_4$ cathode material with 6.10 wt% carbon by the oleic-assisted solid-state route displayed a high specific discharge capacity, good rate performance and superior cycle stability at room and elevated temperature. The superior electrochemical performance of this $LiMn_{0.5}Fe_{0.5}PO_4$/C could be attributed to the presence of a uniform carbon coating layer on the primary particles, an effective conduct network provided by the presence of carbon between the $LiMn_{0.5}Fe_{0.5}PO_4$/C particles, the formation of sufficient pores in the $LiMn_{0.5}Fe_{0.5}PO_4$/C primary particles and aggregates, and the uniform size distribution of the nanoparticles. The facile and scalable solid-state reaction route proposed in the present study is of high efficiency, reliability and high energy-effectiveness, which is promising technique for massive production of high performance $LiMn_{0.5}Fe_{0.5}PO_4$/C cathode material for advanced lithium ion batteries.

## Acknowledgements

This work was supported by the Science and Information Technology of Guangzhou Municipal (2013J4100112, 2014J4500002), the special financial grant from the China postdoctoral science foundation (2013T60795) and the Fok Ying Tung Foundation (NRC07/08.EG01).

## Notes and references

[a] *the Key Laboratory of Fuel Cell Technology of Guangdong province, School of Chemistry and Chemical Engineering, South China University of Technology, Guangzhou, 510640, China; chyfdeng@scut.edu.cn;*
[b] *Centre for Green Products and Processing Technologies, Guangzhou HKUST Fok Ying Tung Research Institute, Guangzhou 511458, China;*
[c] *Department of Chemical and Biomolecular Engineering, The Hong Kong University of Science and Technology, Clear Water Bay, Kowloon, Hong Kong, China, kechengh@ust.hk.*

† Electronic Supplementary Information (ESI) available: See DOI: 10.1039/b000000x/

1 M. Armand and J. M. Tarascon, *Nature*, 2008, **451**, 652–657.
2 P. G. Bruce, B. Scrosati and J. M. Tarascon, *Angew. Chem., Int. Ed.*, 2008, **47**, 2930–2946.
3 W. M. Stanley, *Chem. Rev.*, 2004, 104, 4271–4301.
4 V. Aravindan, J. Gnanaraj, Y.S. Lee and S. Madhavi, *J. Mater. Chem. A*, 2013, **1**, 3518–3539.
5 C. Masquelier and L. Croguennec, *Chem. Rev.*, 2013, **113**, 6552−6591.
6 K. Zaghib, A. Guerfi, P. Hovington, A. Vijh, M. Trudeau, A. Mauger, J.B. Goodenough and C.M. Julien, *J. Power Sources*, 2013, 232, 357-369.
7 C. Delacourt, L. Laffont, R. Bouchet, C. Wurm, J. B. Leriche, M. Morcrette, J. M. Tarascon and C. Masquelier, *J. Electrochem. Soc.*, 2005, **152**, A913–A921.
8 D. Morgan, A. Van der Ven and G. Ceder, *Electrochem. Solid-State Lett.*, 2004, **7**, A30–A32.
9 N. H. Kwon, T. Drezen, I. Exnar, I. Teerlinck, M. Isono and M. Graetzel, *Electrochem. Solid-State Lett.*, 2006, **9,** A277–A280.
10 A. Yamada, Y. Takei, H. Koizumu, N. Sonoyama and R. Kanno, *Chem. Mater.*, 2006, **18**, 804-813.
11 N. Amdouni, K. Zaghib, F. Gendron, A. Mauger and C. Julien, *Ionics*, 2006, **12**, 117-126.
12 M. Kopec, A. Yamada, G. Kobayashi, S. Nishimura, R. Kanno, A. Mauger, F. Gendron and C. M. Julien, *J. Power Sources*, 2009, **189**, 1154-1163.
13 S. K. Martha, J. Grinblat, O. Haik, E. Zinigrad, T. Drezen, J. H. Miners, I. Exnar, A. Kay, B. Markovsky and D. Aurbach, *Angew. Chem. Int. Ed.*, 2009, **48**, 8559–8563.

14 H. L. Wang, Y. Yang, Y. Y. Liang, L. F. Cui, H. S. Casalongue, Y. G. Li, G. S. Hong, Y. Cui and H. J. Dai, *Angew. Chem. Int. Ed.*, 2011, **50**, 7364–7368.

15 G. Yang, H. Ni, H. D. Liu, P. Gao, H. M. Ji, S. Roy, J. Pinto, X. F. Jiang, *J. Power Sources*, 2011, **196**, 4747–4755.

16 S. M. Oh, H. G. Jung, C. S. Yoon, S. T. Myung, K. Amine and Y. K. Sun, J. Power Sources, 2011, **196**, 6924–6928.

17 S. M. Oh, S. T. Myung, J. B. Park, B. Scrosati, K. Amine and Y. K. Sun, *Angew. Chem. Int. Ed.*, 2012, **51**, 1853-1856.

18 W. Liu, P. Gao, Y. Y. Mi, J. T. Chen, H. H. Zhou and X. X. Zhang, *J. Mater. Chem. A*, 2013, **1**, 2411–2417.

19 L. J. Hu, B. Qiu, Y. G. Xia, Z. H. Qin, L. F. Qin, X. F. Zhou and Z. P. Liu, J. Power Sources, 2014, **248**, 246-252.

20 T. Muraliganth and A. Manthiram, *J. Phys. Chem. C*, 2010, **114**, 15530–15540.

21 K. Saravanan, V. Ramar, P. Balaya and J. Vittal, *J. Mater. Chem.*, 2011, **21**, 14925–14935.

22 R. V. Hagen, H. Lottmann, K. C. Moller and S. Mathur, *Adv. Energy. Mater.*, 2012, **2**, 553–559.

23 S. M. Oh, S. T. Myung, Y. S. Choi, K. H. OH, Y. H. Oh and Y. K. Sun, *J. Mater. Chem.*, 2011, **21**, 19368–19374.

24 P. F. Xiao, B. Ding, M. O. Lai and L. Lu, *J. Electrochem. Soc.*, 2013, **160**, A918-A926.

25 Y. J. Zhong, J. T. Li, Z .G. Wu, X. D. Guo, B. H. Zhong and S. G. Sun, *J. Power Sources*, 2013, **234**, 217–222.

26 J. Zong, Q. W. Peng, J. P. Yu and X. J. Liu, *J. Power Sources*, 2013, **228**, 214-219.

27 A. Paolella, G. Bertoni, E. Dilena, S. Marras, A. Ansaldo, L. Manna and C. George, *Nano Lett.*, 2014, **14**, 1477−1483.

28 G. Meligrana, F. D. Lupo, S. Ferrari, M. Destro, S. Bodoardo, N. Garino and C. Gerbaldi, *Electrochim. Acta*, 2013, **105**, 99–109.

29 K. M. Ø. Jensen, M. Christensen, H. P. Gunnlaugsson, N. Lock, E. D. Bøjesen, T. Proffen and B. B. Iversen, *Chem. Mater.*, 2013, **25**, 2282−2290.

30 X. P. Guo, M. Wang, X. L. Huang, P. F. Zhao, X. L. Liu and R. C. Che, *J. Mater. Chem. A*, 2013, **1**, 8775–8781.

31 D. Choi, D. H. Wang, I. T. Bae, J. Xiao, Z. M. Nie, W. Wang, V. V. Viswanathan, Y. J. Lee, J. G. Zhang, G. L. Graff, Z. G. Yang and J. Liu, *Nano Lett.*, 2010, **10**, 2799–2806.

32 L. B. Ran, X. Y. Liu, Q. W. Tang, K. L. Zhu, J. H. Tian, J. Y. Du and Z. Q. Shan, *Electrochim. Acta*, 2013, **114**, 14–20.

33 L. F. Zhang, Q. T. Qu, L. Zhang, J. Li andH. H. Zheng, *J. Mater. Chem. A*, 2014, **2**, 711-719.

34 X. Zhou, Y. F. Deng, L. N. Wan, X. S. Qin and G. H. Chen, *J. Power Sources*, 2014, **265**, 223–230.

35 S. Liu, H. S. Fang, E. R. Dai, B. Yang, Y. C. Yao, W. H. Ma and Y. N. Dai, *Electrochim. Acta*, 2014, **116**, 97–102.

36 P. K. Harold and E. A. Leroy, *X-ray Diffraction Procedure for Polycrystalline and Amorphous Materials*, Wiley, New York, 1974.

37 C. M. Burba and R. Frech, *J. Electrochem. Soc*., 2004, **151**, A1032–1038.

38 M. Maccario, L. Croguennec, B. Desbat, M. Couzi, F. L. Cras and L. Servantd, *J. Electrochem. Soc.*, 2008, **155**, A879–A886.

39 Y. Bai, F. Wu, C. Wu, *Chin. J. Light Scatter*., 2003, **15**, 231–236.

40 J. F. Qian, M. Zhou, Y. L. Cao, X. P. Ai and H. X. Yang, *J. Phys. Chem. C*, 2010, **114**, 3477–3482.

41 C. N. R. Rao, A. K. Sood, K. S. Subrahmanyam and A. Govindaraj, *Angew. Chem. Int. Ed*., 2009, **48**, 7752.

42 H. C. Shin, W. I. Cho and H. Jang, *Electrochim. Acta*, 2006, **52**, 1472-1476.

43 A. Vadivel Murugan, T. Muraliganth and A. Manthiram, *J. Electrochem. Soc.*, 2009, **15**6, A79-A83.

44 R. R. Chen, Y. X. Wu and X. Y. Kong, *J. Power Sources*, 2014, **258**, 246-252.

45 L. Zhang, S. Duan, G. Peng, G. Liang, F. Zou and Y. H. Huang, *J. Alloys Compd.*, 2013, **570**, 61-64.

46 S. L.Yang, X. F. Zhou, J. G. Zhang and Z. P. Liu, *J. Mater. Chem.*, 2010 **20**, 8086-8091.

47 Y. D. Cho, G. T. K. Fey and H. M. Kao, *J. Power Sources*, 2009, **189**, 256-262.

Table 1. Summary of the CV results obtained at different scanning rates and the $Li^+$ diffusion coefficients ($D_{Li}$) determined for the LFMP-S3 electrode.[a]

| Scanning rate ($mV\ s^{-1}$) | Potential values (V) | | | | | |
|---|---|---|---|---|---|---|
| | $E_{pa1}$ | $E_{pa2}$ | $E_{pc1}$ | $E_{pc2}$ | $\triangle E_1$ | $\triangle E_2$ |
| 0.1 | 3.523 | 4.118 | 3.956 | 3.432 | 0.091 | 0.162 |
| 0.2 | 3.570 | 4.141 | 3.933 | 3.414 | 0.156 | 0.208 |
| 0.3 | 3.570 | 4.158 | 3.933 | 3.414 | 0.156 | 0.225 |
| 0.4 | 3.578 | 4.167 | 3.924 | 3.414 | 0.164 | 0.243 |
| 0.5 | 3.587 | 4.167 | 3.916 | 3.404 | 0.183 | 0.251 |
| 1.0 | 3.665 | 4.228 | 3.881 | 3.379 | 0.287 | 0.347 |
| $D_{Li}^+$ ($\times 10^{-11}$ cm $s^{-1}$) | 11.00 | 1.73 | 1.72 | 3.46 | | |

[a] $E_{pa}$: anodic peak potential, $E_{pc}$: cathodic peak potential, $\Delta E$: the separation between $E_{pa}$ and $E_{pc}$. The subscript numbers 1 and 2 denote the redox couple at lower and higher potential, respectively.